Progress in Additive Manufacturing
https://doi.org/10.1007/s40964-025-01111-7

RESEARCH

Comparative thermal analysis, design, and structural assessment of lattice-based additively manufactured heat pipes for space applications

Giovanni Brambati[1] · Luigi Vitali[2] · Manfredo Guilizzoni[2] · Emmanuel Caplanne[3] · Alfonso Niro[2] · Stefano Foletti[1]

Received: 25 November 2024 / Accepted: 5 April 2025
© The Author(s) 2025

Abstract

This paper details the thermal design and the mechanical assessment procedures for an additively manufactured AlSi10Mg heat pipe, incorporating lattice structures as a wick for the cooling of a satellite power unit's electronics. To optimize thermal performance, various lattice structures were experimentally investigated, focusing on properties, such as capillary rise, permeability, and heat removal capabilities. The best-performing lattice structure was further analyzed for its static and fatigue properties. A fatigue life model, comprising the experimental data on the lattice and SN diagrams for the bulk material obtained from propagation law, is presented. A sample representative of the heat pipe was designed and experimentally tested to validate the predictive capability of the fatigue life model and to assess the structural integrity of the heat pipe against the loading conditions experienced during a space launch. The heat pipe design demonstrated the ability to remove 24 W at 0° inclination, a near-isothermal functioning at 18 W up to an inclination of 15° angle, corresponding to a 34 mm height counter-gravity. The component demonstrated the capability to withstand the stresses resulting from nine repetitions of the space launch, confirming the model's predicting capability.

Graphical abstract

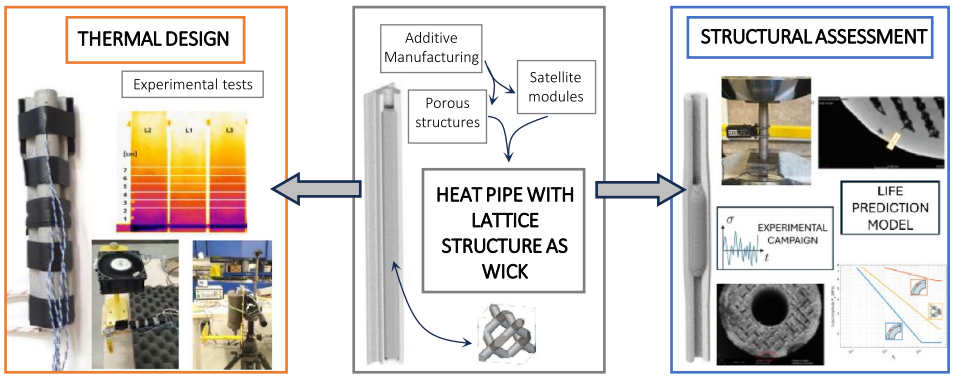

Keywords Heat pipe · Thermal analysis · Structural assessment · Lattice structures · AlSi10Mg

Abbreviations

AM	Additive manufacturing
CT	Computed tomography
DOE	Design of experiments
HP	Heat pipe
LEVD	Large extreme value distribution
PBF-LB/M	Laser powder bed fusion of metals
PSD	Power spectral density
RMS	Root mean square
RS	Residual stresses
SEM	Scanning electron microscope
SN	Stress—life diagram
UTS	Ultimate tensile strength

Extended author information available on the last page of the article

Published online: 12 May 2025

Greek symbols

ϕ	Inclination angle (°)
ρ	As-manufactured relative density (–)
ρ_f	Fluid density (kg/m^3)
ρ_l	Lattice relative density (–)
σ	Nominal stress (MPa)
σ_f	Fluid surface tension (Pa)
θ	Contact angle between fluid and material (°)

Symbols

ΔK_{th}	Long crack threshold SIF (MPa m$^{0.5}$)
ΔP_c	Pressure difference of capillary forces (Pa)
ΔP_h	Pressure head due to gravity (Pa)
Δz	Capillary height (mm)
a	Crack depth (mm)
c	Semi-crack length at surface (mm)
C_l	Lattice unit cell length (mm)
D	Miner's damage index (–)
d_s	Lattice strut diameter (mm)
E	Young's modulus (MPa)
F	Correction factor for the SIF (–)
f_N	Newmann's opening function (–)
g	Gravity constant (m/s^2)
K	Stress instensity factor (SIF) (MPa m$^{0.5}$)
K_f	Permeability (μm^2)
N_f	Cycles to failure (–)
P	Input power (W)
R	Stress ratio (–)
r	Radius of the capillary tubular channel (mm)
r_p	Equivalent pore radius (mm)
r_s	Inscribed sphere radius (mm)
R_v	Roughness valley depth (mm)
T	Temperature (°C)

1 Introduction

As electronic devices become more powerful and compact, efforts to add them to satellites are increasing; however, managing the heat generated by these devices and prevent the formation of 'hot spots', that would impact electronics' reliability [1], has emerged as a significant engineering challenge. Consequently, research into integrating heat pipes into satellite structures has gained attention in the past, for which a comprehensive overview is present in the work of Shukla et al. [2], and more recently, the need of including devices aimed at improving the temperature control has been further expressed in the work of Ghidini et al. [3]. Capillary-driven heat pipes are crucial components in the thermal management of electronic devices [4], particularly in environments where efficient heat dissipation is critical, such as space components [2]. Heat pipes (HP) consist of a sealed container, whose inner surface is covered with a porous structure, called wick [2]. The container is partially filled with a working fluid, that is chosen depending on the application. The working fluid heated on one side of the heat pipe by an heat source evaporates, and the vapor moves to the other end of the HP, the condenser, where the vapor returns to its liquid form. The function of the wick material on the inner surface of the heat pipe is to guide the condensated fluid back to the evaporator, thanks to the action of capillary forces [5]. Although wick structures made with the conventional methods, such as sintered metal powders or grooved designs, continue to be a focus of research [6], they present limitations in terms of manufacturing complexity and performance under different orientations and conditions. Additive manufacturing, especially Laser-Based Powder Bed Fusion of Metals (PBF-LB/M), offers a promising alternative by enabling the creation of complex internal geometries, tailored to specific thermal and capillary requirements [7], and enabling the possibility of manufacturing satellite's modules with embedded heat pipes. In recent years, numerous studies have explored the manufacturing of heat pipes with wicks made from various types of porous structures obtained through additive manufacturing. Some studies have focused on achieving sintered-style porous structures, such as the work by Jafari et al. on stainless steel [8–10] on aluminum, which evaluated thermo-fluid characteristics, including porosity, permeability, and capillary rise. Other research has concentrated on architected cellular structures, such as lattice structures. Ameli et al. [11, 12] used a design of experiments (DOE) approach to assess the characteristics of both random and architected porous structures, later testing a heat pipe capable of dissipating 16 W and operating against gravity up to a height of 60 mm. Subsequent studies, such as that by McGlen et al. [13], focused on titanium-based heat pipes with lattice wicks, achieving a dissipating power of 30 W at counter-gravity angles of 20°. While previous research has largely focused on the thermal performance of heat pipes, it is equally important to assess the mechanical strength of these components, when considering the case of a space application. The qualification and structural integrity assessment of additively manufactured components pose greater challenges compared to traditional ones [14]. Several studies have investigated structural integrity at the material level, focusing on Processing–Structure–Properties–Performance relationship [15], but also at the component level [16–18], including the work of Gavazzoni et al. [19], who conducted a structural assessment of a component with a bulk-lattice hybrid architecture for a space application.

To the best of the authors' knowledge, no prior studies have presented a comprehensive overview of the design of a AM heat pipe with lattice structure as wick from both thermal and mechanical point of view, with also an assessment against random vibration induced by a space launch.

1.1 Design requirements

This research activity is part of the ESA ARTES Advanced Technology Program, which supports technological advancements in the satellite sector. The design requirement specifies that a single heat pipe must dissipate at least 20 W-equivalent to the heat typically managed by a conduction-only module in a conventional power unit. The integration of multiple heat pipes within a single power module highlights the potential enhancement in thermal management offered by this innovative solution. The heat pipe is considered to function properly if the temperature difference along its length is below 15 °C. From a mechanical standpoint, structural integrity must be ensured for at least seven repetitions of a space launch load history, in compliance with ECSS E-ST-32-01C [20] guidelines. Based on these requirements, the research activity is structured as follows: in Sect. 2, a comparison of various lattice structures in terms of fluidic characteristics will be described, while the HP's thermal performances are reported in Sect. 3, in both 0° orientations—simulating a micro-gravity environment—and counter-gravity conditions for on-Earth functioning. The best-performing heat pipe is mechanically assessed in Sect. 4, with the use of a life prediction model and with experimental tests performed on component-like specimens.

2 Comparative characterization of lattice structures

The design phase began with a comparative experimental analysis of various lattice structures to identify the most effective wick for the heat pipe. The evaluation metrics included permeability and capillary rise. Permeability (K_f) was selected as an indicator of the volumetric component of heat transfer: higher permeability allows greater fluid passage, enhancing heat dissipation. Capillary rise was used as a metric for the against-gravity performance of the heat pipe. Three lattice variants, differing in unit cell length (C_l) and strut diameter (d_s), were considered (Fig. 1), while keeping constant the diamond lattice topology for all cases. The strut length inside the topology is represented by the node–node length and all the struts in the topology have an angle of 35.25° with respect to the build platform [21]. By varying unit cell length and strut diameter, it was possible to influence two geometrical parameters: the inscribed sphere radius (r_s) and the lattice relative density (ρ_l). The parameter r_s was varied to investigate different capillary rises. Following equilibrium in pressure difference imposed by (Eq. 1) and gravity (Eq. 2) [8], a smaller sphere radius should correspond to a higher capillary rise

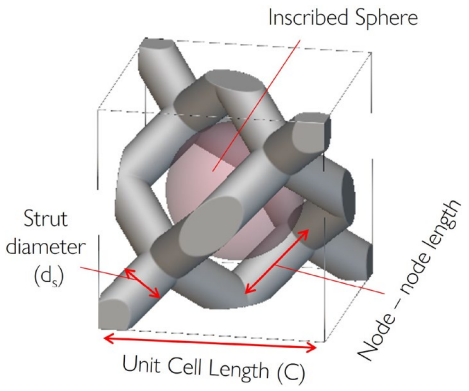

Fig. 1 Diamond lattice unit cell with geometrical quantities of interest

$$\Delta P_c = \frac{2\sigma_f \cos\theta}{r_s} \tag{1}$$

$$\Delta P_h = \rho_f g \Delta z. \tag{2}$$

In Eq. (1), σ_f is the fluid surface tension, θ is the contact angle between the fluid and the material and in Eq. (2) ρ_f is the fluid mass density, g is the gravity constant, and Δz is the capillary height. Experimental capillary rate-of-rise tests were performed on a dedicated specimen (Fig. 2a) to measure the actual capillary rise. The equivalent pore radius (r_p) was computed experimentally, as shown in [8, 22], as a measure of the value of capillary rise. Permeability is measured with dedicated specimens, showed in Fig. 2b, with the same experimental procedure outlined in [22]. Acetone was selected as the testing fluid for all experiments due to its thermo-fluid dynamics properties, which closely resemble those of ammonia—the desired coolant for the satellite's power unit—while avoiding ammonia's toxicity. All specimens used in this study were printed in AlSi10Mg using a GE Additive M2 Series 5 printer by BeamIt S.p.A. (Fornovo di Taro, PR, Italy). The printing parameters for all specimens included a volumetric energy density (VED) of 33.88 W/mm^3, a laser power of 370 W, and a layer thickness of 60 µm. A contouring scanning strategy was used to ensure high geometrical precision and surface finishing, as all specimens were intended to remain in their net-shape condition. All the samples were produced on a preheated build plate at 150 °C and subjected to a stress-relief heat treatment at 200 °C for 4 h after printing.

From the experimental results presented in Table 1, the following conclusions can be drawn regarding the different lattices investigated:

- L1 Exhibited very low permeability, as expected from its high relative density and showed the lowest capillary

rise, highlighted by the larger equivalent pore radius. This is not expected as its r_s value was the lowest among the three. This could indicate a poor interconnectivity between its pores and presence of occluded ones that prevent fluid capillary rise.

- L2 and L3 showed similar results both in terms of capillary rise and permeability. However, when the capillary rise specimens were slightly inclined, the fluid in the L3 lattice fell due to gravity, demonstrating the lattice's inability to effectively retain the fluid under such conditions.

3 Heat-pipe design and thermal testing

Heat pipes were printed with the three different lattices (L1, L2, L3) presented in Sect. 2, with the same process parameters employed for the permeability and capillary rise specimens. The technical drawing of the heat pipe is presented in Fig. 3. A heat pipe with a reduced cross-section was also printed, to test a configuration more suitable for the confined space of a satellite's power unit. Table 2 lists the geometrical parameters of the two cross-sections. The heat pipe with reduced cross-section has L2 lattice as wick, and will be indicated as L2R. The flat surface is used to mimic

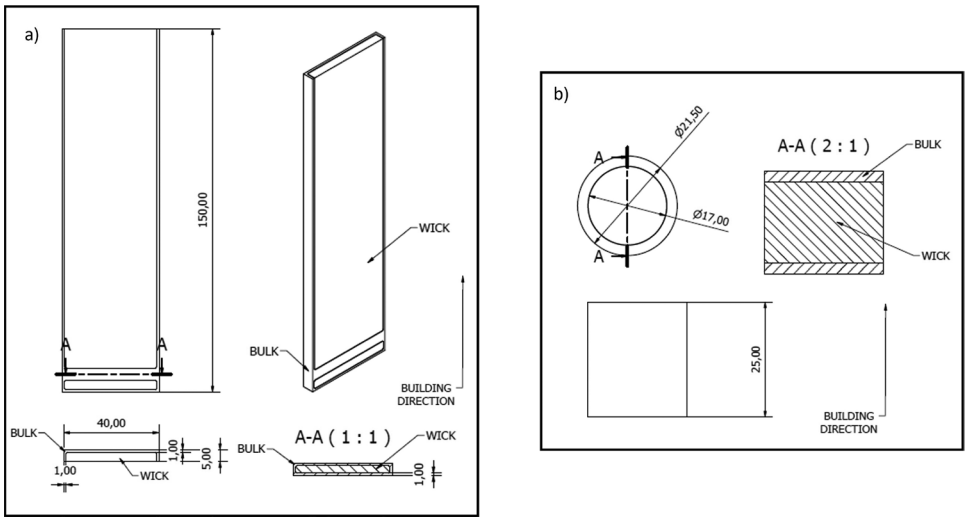

Fig. 2 Technical drawings of the specimens used for the lattice evaluation: **a** capillary rise specimen and **b** permeability specimen

Table 1 Properties of the printed lattice porous structures

	Unit cell length (mm)	Strut diameter d_s (μm)	Node–node length (mm)	Lattice relative density ρ_l (%)	Sphere radius r_s (μm)	Equivalent pore radius* r_p (μm)	Permeability* K_f (μm^2)
Lattice 1 (L1)	1.30	660	0.56	65	200	98.3	16
Lattice 2 (L2)	1.38	600	0.60	55	265	86.8	238
Lattice 3 (L3)	1.50	600	0.65	50	310	86.8	260

Values with asterisk (*) are experimentally measured [23]

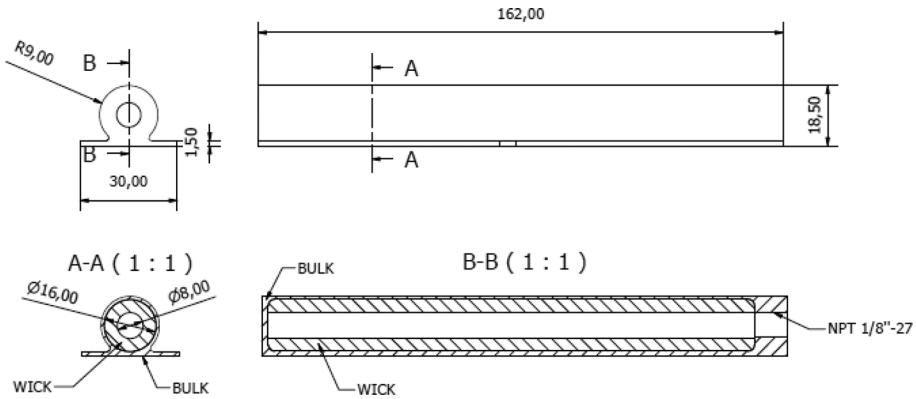

Fig. 3 Technical drawing of the heat pipe used for thermal testing

the electronic module in Fig. 18, and to ease the mounting of the resistors and heat sink. In correspondence of the heat pipe's opening, a threaded junction (NPT 1/8-27) was manufactured to feature a ball valve for the fluid filling and sealing. To evaluate thermal performance, a test rig was constructed to test the heat pipes under heat loads in various orientations. Thermocouples were uniformly placed along the heat pipe to record temperature data, the power input was carefully controlled with the use of resistors, and it is dissipated with forced convection by the use of a fan and a finned surface (Fig. 4a). The test rig, depicted in Fig. 4b, and the testing procedures are thoroughly described in [23]. The effective length considered in the thermal testing is 130 mm, that is the total length of the specimen minus the region of the evaporator and the condenser. The heat pipe's effectiveness was measured by the temperature gradient (ΔT) along the length of the pipe, defined as the difference between the temperature at the evaporator and the last thermocouple before the condenser. An ideal heat pipe exhibits a temperature difference close to zero along its length, thus acting as a zero-resistance thermal conductor. In this study, the heat pipe was considered to function properly if ΔT remained below 15 °C. In addition, results are compared with the same heat pipe acting as a pure conductor, i.e., without a working fluid inside, corresponding a total uncorrect functioning. For the different heat pipes, the results will be graphically presented with plots in terms of ΔT with respect to power input P or inclination angle ϕ. The capillary rise is related to the inclination angle by the product between the effective length and the sine of the inclination angle. To represent a micro-gravity condition during the test, the heat pipe inclination was kept between − 0.5° and − 1.5° (in the text, this will be referred as 0-°), so that gravity does not positively affect the obtained results.

Figure 5 presents the results of the heat pipes with respect to the inclination angles for various input powers. Additionally, results obtained by some heat pipes tested empty are also reported to give information of the worst case scenario, i.e., the heat pipe acting as mere conductor. The thermal testing of L1 heat pipe confirmed the results presented in Sect. 2, which is not able to reduce the temperature difference between the evaporator and the condenser in against-gravity condition, even for low power input. Notably, from -10°, the temperature difference profile remains constant, indicating a behavior similar to a pure conductor. Compared with the other configurations, the heat pipe with lattice L2 exhibited the best performances at high input power for angles higher than -20°, in correspondence of which a sharp

Table 2 Values of the geometrical parameters for the original and reduced cross sections

	Large	Reduced
External bulk diameter (*mm*)	18	14
Internal bulk diameter (*mm*)	16	12
Internal wick diameter (*mm*)	8	5.4
Wick thickness (*mm*)	4	3.3
plate thickness (*mm*)	1	1.5

Original cross-section showed in Fig. 3

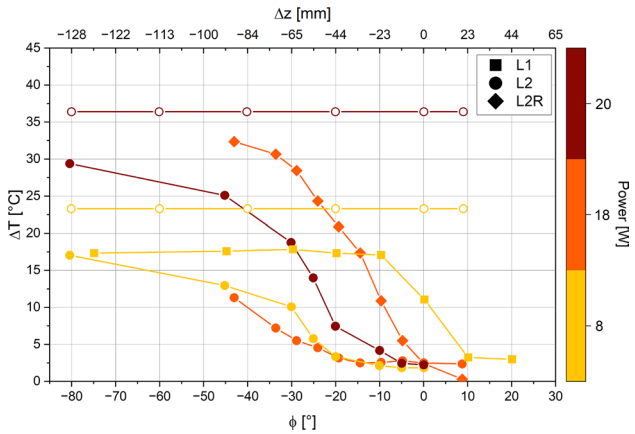

Fig. 5 Results of different heat pipes with respect to the inclination angles and for the input powers tested. Empty symbols refer to a condition of empty heat pipe, acting as pure conductor. The nomenclature L1, L2 refer to Table 1 and R is for the reduced cross-section

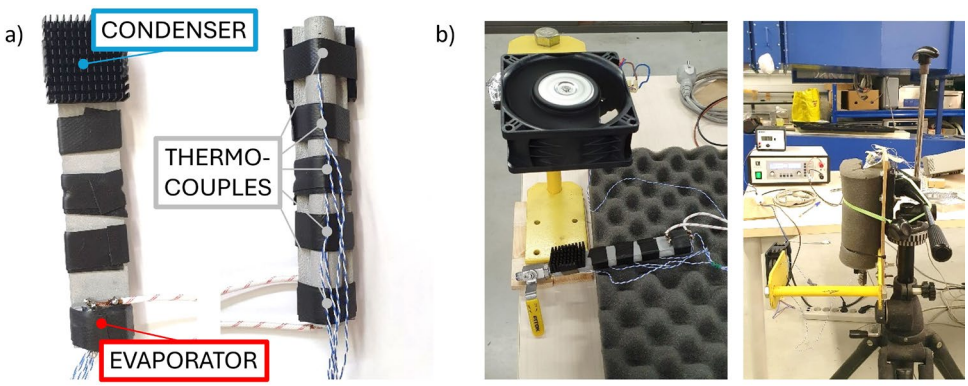

Fig. 4 Test rig used for the heat pipes' thermal testing [23]. **a** Focus on the heat pipe thermocouples, resistor, and heat sink. **b** Test rig for evaluate the heat pipe at different inclinations

increase in ΔT was observed. A slight dryout at the evaporator, indicated by a rapid increase in temperature difference, was detected at $\phi = -10°$ for 20 W. This behavior is also present, in a less pronounced way, at 8 W. L2R heat pipe experiences earlier dryout and higher temperature differences with respect to L2. It can be graphically seen in Fig. 5 that for an input power of 18 W L2R ΔT curve rises more rapidly than the one of the larger cross-section, indicating a non-optimal heat pipe behavior even at $-15°$. This can be attributed to both the reduced wick section, reducing fluid mass transport capabilities and evaporative surface area, and the overall mass reduction, consisting in a 55% decrease in the thermal conductance. While this reduction is hidden when the heat pipe operates within its optimal range (where heat is dominantly conducted through the working fluid), it becomes evident as soon as the heat pipe deviates from its effective operating window. Moreover, the lower thermal conductance of the structure may increase localized heat loads, further aggravating dryout issues. The influence of input power is examined in Fig. 6. At 0-°, L2 HP maintained a stable temperature difference up to 30 W, while at $-10°$, the evaporator partial dryout can be seen by the linear trend of ΔT. Evaporator partial dryout can be seen also at 0-° for the L2R case, where the 15 °C limit is reached for a 24 W power input. Comparing the ΔT of L2 and L2R empty HP in Fig. 6, their ratio is approximately 1.4, aligning with the thermal conductance ratio of the two heat pipes. L3 HP was expected to show similar, if not better, performance compared to L2, since L3 is characterized by a higher porosity. However, an unstable behavior in time was observed during the testing. Figure 7 illustrates the measured ΔT for a $-5°$ inclination angle in time and compares it with the same case of L2 HP, which shows a convergence in time of the temperature difference. In Figs. 5 and 6 L3 HP was not taken into consideration, since there are no steady-state results available. As mentioned in Sect. 2, it is likely that the capillary forces acting between the liquid and the lattice are overcame by the weight of the fluid in a counter-gravity configuration, which induce the fluid to periodically fall before reaching the evaporator. The conducted tests show the following:

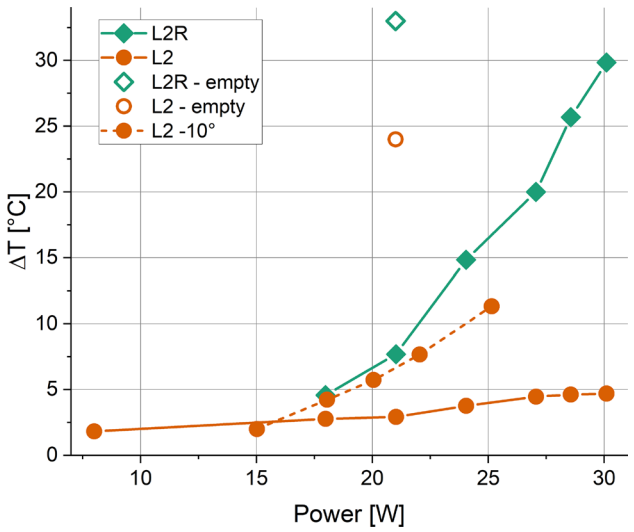

Fig. 6 Results of different heat pipes (L2 and L2R) with respect to input power at 0-° (solid line) and one case at $-10°$ (dashed line). Empty symbols refer to a condition of empty heat pipe, acting as pure conductor

- L2 HP demonstrated the best performances in therms of ΔT reduction. At 0-°, input powers up to 30 W induced temperature differences less than 3 °C, and against-gravity correct functioning was seen up to $-20°$ for 20 W. The geometrical dimensions of L2, however, prevent its application to a satellite's power unit.
- L2R correct functioning is assessed for input powers lower than 24 W at 0-°, and up to $-15°$ inclination angles for 18 W.

Fig. 7 ΔT with respect to time in L2 and L3 heat pipes inclined at $-5°$

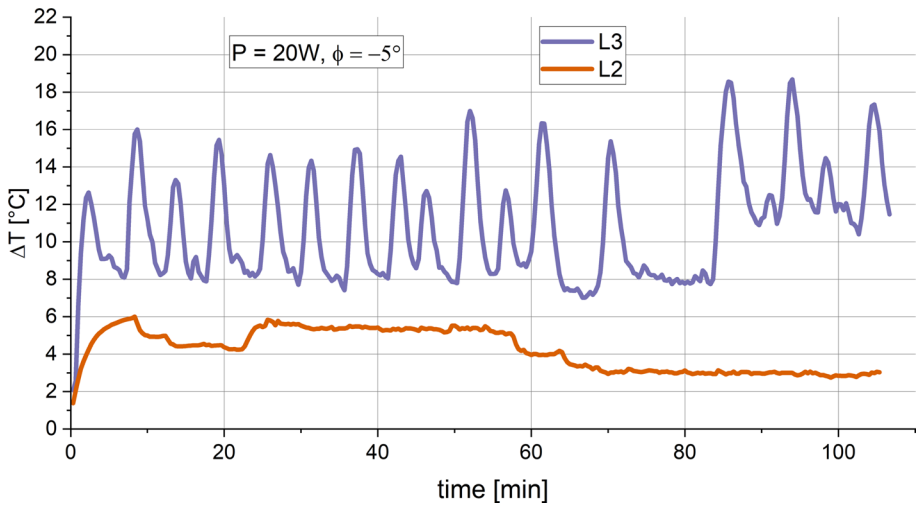

- L1 HP is not suitable to be implemented in the satellite's power unit, as it shows unsatisfactory results even at low inclination angles.
- L3 HP is not suitable to be implemented in the satellite's power unit, as it shows an unstable behavior in against-gravity condition.

4 Heat-pipe structural prediction and assessment

In the design process of the heat pipe, it is crucial to predict its structural resistance to random vibrations caused by the space launch. The prediction and assessment are based on a component-like specimen, that can be seen in Fig. 8 and is introduced in Sect. 4.3. The life prediction model is based on the assumption that fatigue cracks can originate in three locations: in the bulk material external and internal surface and within the lattice. While localized failure in the wick would not significantly affect thermal performance, this could lead to stress concentration that acts as stress raiser, facilitating crack initiation and propagation in the bulk material. To predict the life of the heat pipe, it is therefore necessary to know which of these three locations is the critical one and to assess the component based on that information. Each potential failure site requires a dedicated stress-life (SN) diagram. For the two cases concerning the bulk material, the SN diagrams were obtained by integrating a crack propagation law with information on defect size, surface roughness and residual stresses coming from analysis on component-like specimen (Sect. 4.1) [18]. Since no tools are available to predict the SN diagram of the lattice structure, an experimental activity was performed on dedicated specimen and the results are presented in detail in Sect. 4.2. With the life prediction model, the heat pipe's life can be predicted by computing the damage from a space launch load history. The component-like specimens were tested at constant and variable amplitude fatigue, to validate the prediction model and to assess the structural integrity. The workflow of the life prediction and assessment is outlined in Fig. 8.

4.1 Life prediction model for the bulk material

A crack propagation equation 3 is considered, where the material properties from the literature are combined with the actual characteristics of the component, such as defects, surface roughness, and residual stresses, coming from analysis on the component-like specimen [18]. The integration of the crack propagation law from an initial crack size up to a final crack length allows the obtaining of SN diagrams relative to the bulk part of the component. The crack propagation law considered is a NASGRO-type equation

$$\frac{da}{dN} = C \cdot \left[\left(\frac{1 - f_N}{1 - R_{\text{eff}}} \right) \cdot \Delta K \right]^n \cdot \left(1 - \frac{\Delta K_{\text{th}}}{\Delta K} \right)^p . \tag{3}$$

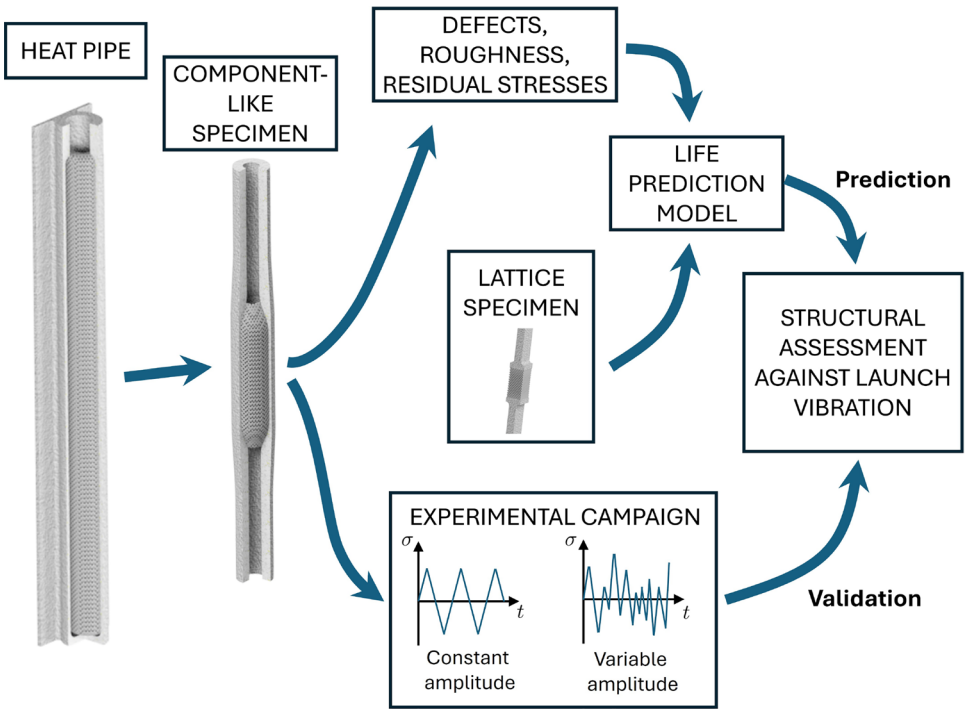

Fig. 8 Workflow of the structural prediction and assessment of the heat pipe against space launch vibrations

In Eq. (3), C, n, and p are material parameters, f_N is Newman's crack opening function [24], R_{eff} is the effective stress ratio, ΔK is the stress intensity factor range, and ΔK_{th} is the short crack threshold stress intensity factor range, computed with the Kitagawa-Takahashi diagram, built with the model proposed by El-Haddad [25]. Material properties are taken from [18], where the functions for determining f_N and ΔK_{th} are also presented. The stress intensity factor K, and its relative range ΔK, are computed as

$$K = F(a, c)\sigma\sqrt{\pi a}, \tag{4}$$

where $F(a, c)$ is the correction factor for semi-elliptical surface cracks in hollow cylinders [26], σ is the applied stress, and a is the crack depth.

The initial value of the crack, necessary for the integration of Eq. (3), was taken from a defects' characterization of the component-like specimen, performed with high-resolution CT-scans (100 kV, 140 µA Phoenix-X-ray system, with a voxel size of 12 µm) of a sample's gauge section. The CT-scans were analyzed to detect the defects using the *Easypore* module of the commercial software VGStudioMax®. For the external surface, the critical defect was identified as the one with the largest projected area in the plane transversal to the applied load (Fig. 9b). The critical defect, highlighted in Fig. 9c, was modeled as a semicircular crack with an initial size a = c = 0.35 mm equal to the defect depth.

For the bulk material's internal surface, the focus was placed on the surface roughness, which is worsen due to the presence of the lattice structure. Previous studies have demonstrated that roughness can act as a fatigue crack initiator [19, 27]. To evaluate the surface roughness in such complicated geometries, the following procedure has been employed. First, the CT-scan images have been binarised to discriminate material and voids and obtain a 3D reconstruction of the internal surface without the lattice structure. Using Materialize 3-matic®and its *Part Comparison* tool, the distances from the reconstructed bulk internal surface mesh to the nearest points on the as-designed cylindrical internal surface were computed. The values obtained are characterized by a mean of 0.023 mm, a standard deviation of 0.019 mm, and a maximum value of 0.24 mm. Following the methodology of [27], a maximum roughness depth was selected as initial defect size for fatigue life estimation (Fig. 10).

As previously mentioned, for a correct transferability from specimen to component, it is necessary to take into account also residual stresses present in the component. As reported in [28], residual stresses may still be present in AM-AlSi10Mg parts even after stress-relief treatments, such as the one employed in this case (Sect. 2). Tensile residual stresses, in particular, can be detrimental to fatigue life, since they alternate the stress ratio, introducing a positive mean stress component. Residual stresses in the component-like sample were measured using an X-Stress 3000 AST portable X-ray diffractometer (2 mm-diameter collimator, CrKα1 radiation), with measurements taken from the surface to a maximum depth of 0.3 mm with 0.1 mm increments.

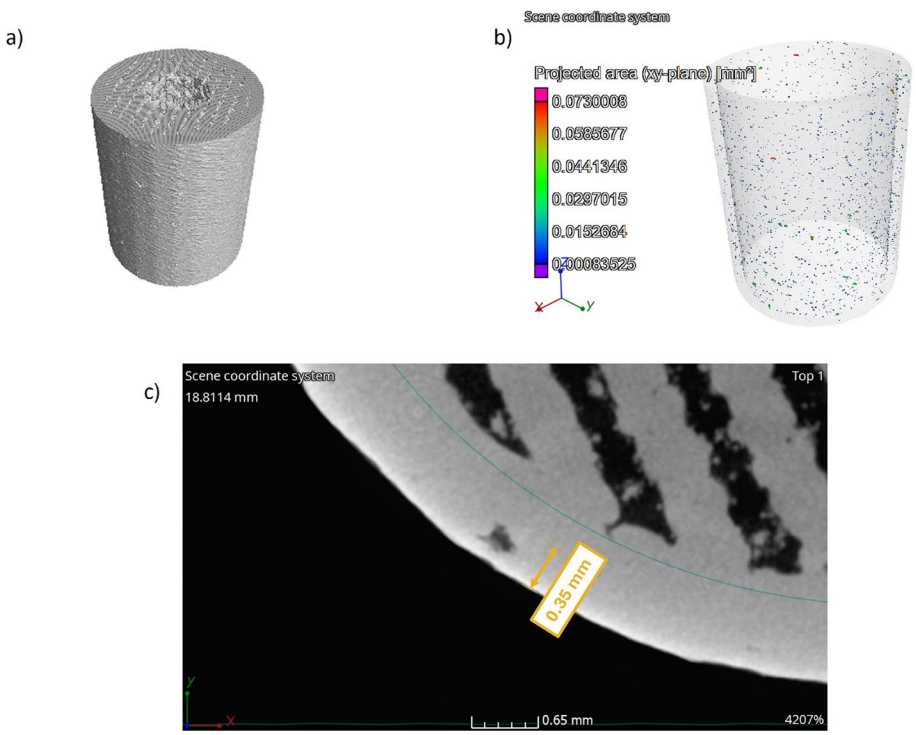

Fig. 9 CT-scans analysis for the estimation of external defects. **a** 3D reconstruction of the scanned volume, **b** results of the *Easypore* analysis, and **c** critical defect considered

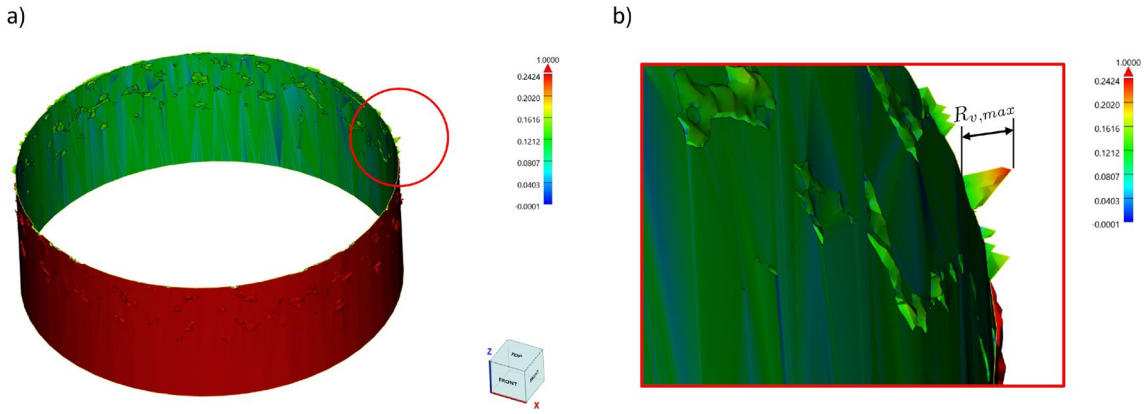

Fig. 10 CT-scans analysis of the internal surface roughness. **a** 3D reconstruction of the internal volume and **b** maximum R_v considered

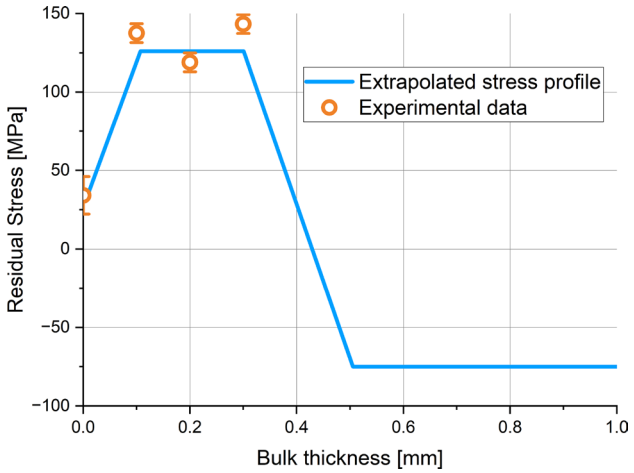

Fig. 11 Approximated profile of residual stresses in the longitudinal direction with experimentally measured data-points

To evaluate the residual stresses in the remaining part of the component, the method proposed by Smith et al. [29] was used. The method is based on the assumption that residual stresses are self-balanced in a cylindrical domain, allowing for an approximated profile to be computed, based on momentum and force equilibrium equations. In Fig. 11, the residual stress measurements in the specimen's longitudinal direction are depicted, alongside the computed profile in the thickness. It is assumed that only the bulk material is capable of carrying residual stresses, since no experimental activity proved the existence of residual stresses in lattice structures. In addition, tensile residual stresses were assumed to decrease after the last measured point (0.3 mm). In Eq. (3), the residual stresses are introduced in the R_{eff} term [30] with the following equation:

$$R_{\text{eff}} = \frac{K_{\min}(a) + K_{RS}(a)}{K_{\max}(a) + K_{RS}(a)}, \tag{5}$$

where $K_{\text{min,max}}$ are the minimum and maximum stress intensity factor during fatigue loading and K_{RS} is the stress intensity factor due to the residual stress state.

Finally, to integrate Eq. (3) and obtain the SN diagram, it was necessary to define a final crack size. Given that the heat pipe contains an internal fluid, the final crack depth must be lower than the bulk thickness to prevent fluid leakage. The following conditions are set as final crack size: the crack depth a must be less than half the bulk thickness (0.5 mm), and the half the crack length at the surface c must be less than the bulk thickness (1 mm).

Figure 12 presents the SN diagrams obtained for bulk's external and internal surface. As it can be noted by the position of the dashed lines, that represent the SN diagram without considering residual stresses, the presence of tensile residual stresses plays a crucial role, leading to a marked difference in the life between the external and internal surface of the heat pipe.

4.2 Experimental investigation of lattice mechanical properties

The mechanical properties of the lattice structure were investigated with a dedicated experimental activity. The lattice specimen used in the test was designed using the commercial software nTopology®[31], and it is shown in Fig. 13. The specimen has a cubic gauge section with 7 unit cells in each side with a uniform relative density ($\rho = 55\%$). Three rows of graded-density unit cells have been interposed between the ends of the gauge section and the grip regions: these unit cells have an increasing strut diameter, which helps to mitigate stress concentration and reduce the likelihood of failure at the interface between

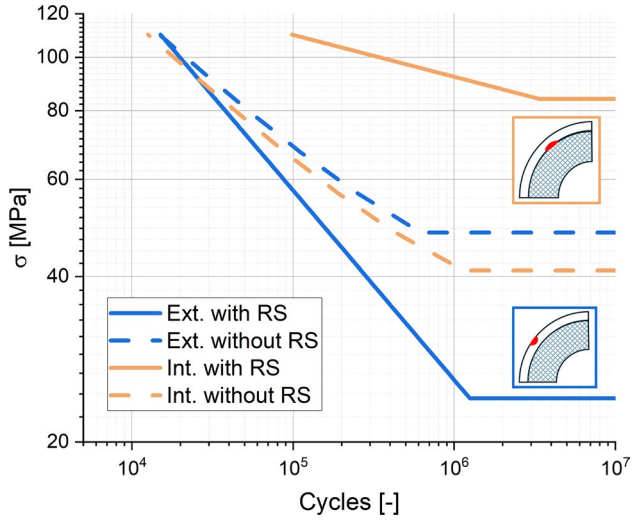

Fig. 12 SN diagrams of the bulk material for the case of heat pipe component. External and internal cracks presented with dashed lines for the case without considering residual stresses

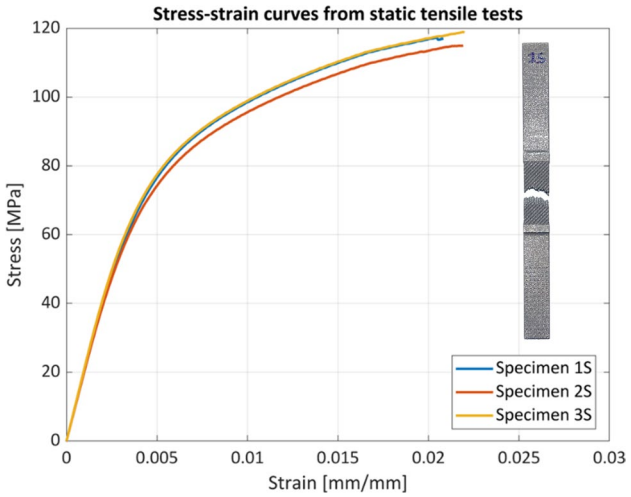

Fig. 14 Stress–strain curves of the lattice specimens with picture of a broken sample

the lattice material and the bulk material of the grips during experimental testing. The number of unit cells and the design of the transition regions were selected based on guidelines from [32] to avoid scale effects and ensure a statistically significant number of cells for the study of fatigue properties [33]. The building direction for this specimen is reported in Fig. 13b.

Static tension tests were conducted on three specimens following the guidelines of ASTM Standard E8/E8M [34]. The tests were conducted at a given cross-bar speed of 1 mm/min and monitored with a 10 mm extensometer. The resulting stress–strain curves are presented in Fig. 14 where the stress considered is the homogenized stress, i.e., the stress seen by an equivalent homogeneous material, computed as the force divided by specimen's area (Table 3).

Experimental fatigue tests have been performed on the lattice specimens with a Instron E10000 testing machine at a frequency of 30 Hz. To study the fatigue behavior under conditions simulating launch vibrations, which are assumed to follow a Gaussian distribution with a zero mean value, all fatigue tests were conducted in tension compression with a stress ratio of $R = -1$, so as to achieve a mean stress value equal to zero. The test campaign was conducted in accordance with the standard ASTM 739 [35] and to determine the SN curve for the finite fatigue life, three stress levels (30, 18, and 12 MPa) have been defined. Four tests for each stress level were conducted, thus leading to a replication index of 75%, compliant for design allowable data. The data coming from the testing machine have been analyzed to determine the number of cycles to failure (N_f). This was identified as the intersection of the stiffness data with a linear interpolation of the stiffness decay in the region of linear decrease, shifted downward by 2%. The experimental data are fitted

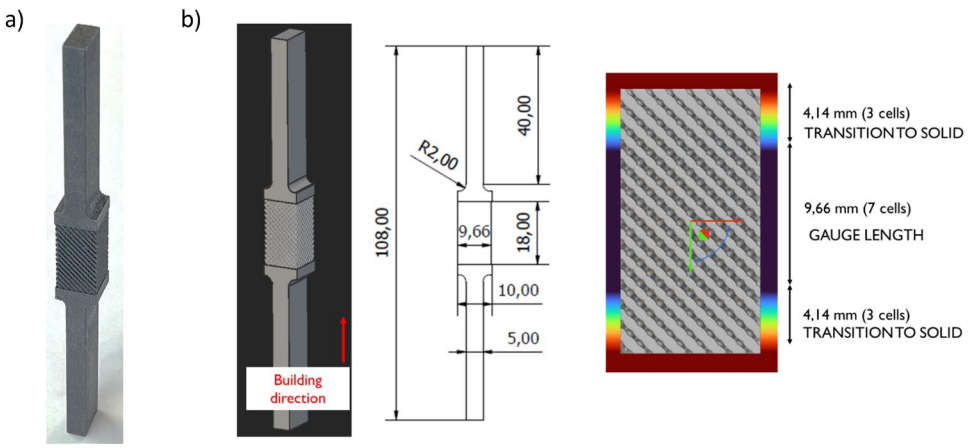

Fig. 13 Lattice specimen for mechanical testing: **a** printed specimen and **b** technical drawings and highlights of the transition regions

Table 3 Lattice tensile tests results

	Mean	SD
E (MPa)	20782	508
σ_y (MPa)	82.2	1.8
UTS (MPa)	117	2.0
ϵ_f (mm/mm)	0.0219	6.6e−4

with a linear regression in the double logarithmic plane, with the following relation:

$$\log_{10}\left(N_f\right) = b_0 + b_1 \log_{10}\left(\sigma_a\right). \tag{6}$$

The standard deviation of the dependent variable $\sigma_{\log N}$ is computed as

$$\sigma_{\log N} = \sqrt{\frac{\sum_{i=1}^{n}\left(Y_i - \hat{Y}_i\right)^2}{n-p}}, \tag{7}$$

where n is the number of samples, p is the number of estimated parameters (2 in this case), Y_i is the base 10 logarithm of the number of cycles to failure of the ith observation, and $\hat{Y}_i$ is the base 10 logarithm of the model estimate number of cycles to failure. The experimental data, the regression curve, and the 95% scatter band are presented in Fig. 15, while the values of b_0, b_1, and $\sigma_{\log N}$ are reported in Table 4.

The fatigue limit was estimated using Dixon's method [36], which requires a minimum of six tests. Three stress levels were selected with a fixed step of 2 MPa, corresponding to the standard deviation of the SN curve data. The run-out condition was set at 5×10^6 cycles. The test results are presented in Table 5 and the resulting fatigue limit in Table 4.

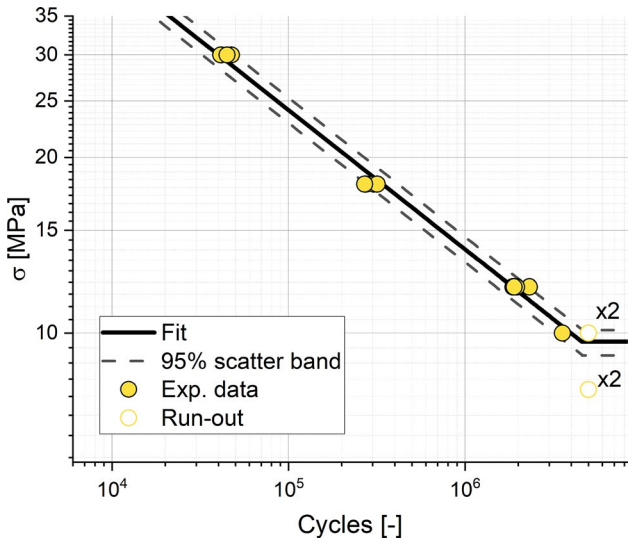

Fig. 15 SN diagram for the lattice specimen

Table 4 Fitting parameters of the lattice fatigue tests results

b_0	10.75
b_1	− 4.16
$\sigma_{\log N}$	0.063
$\sigma_{\lim}$	9.67 MPa

4.3 Fatigue life prediction

This section introduces the component-like specimen (Fig. 16), which, in the gauge length, replicates the geometry of L2R heat pipe thermally tested in Sect. 3.

Given that the specimen is composed of both bulk and lattice material, it is essential to understand the load distribution between the two. The specimen was modeled in a finite-element analysis, where the lattice structure was considered as a homogeneous isotropic material, with stiffness derived from tensile tests presented in Sect. 4.2. Bulk material properties were taken from the literature [18]. A tie constraint was applied at the bulk–lattice interface to ensure displacement continuity. To resemble the conditions of the tested specimens, the bottom face was fixed, while the top face was kinematically coupled to a reference point, placed on the axis of the specimen, where the displacement is applied. Considering an applied load of 1 kN on the reference point, it is possible to know that the load applied to the component is distributed 14.47 MPa/kN in the bulk material and 4.54 MPa/kN in the lattice. For a given load applied to the heat pipe, it is possible to compute the stress acting on the bulk and the lattice, and from the relative SN diagrams in Figs. 12 and 15, it is possible to determine the critical location for the life prediction of the heat pipe. Figure 17 reports the predicted load-life diagram of component-like specimen, for the different failure locations assumed. The line representing failure from the external bulk surface is the most critical one, being the one with the lowest number of cycles to failure for any given load.

4.3.1 Space launch damage prediction

Figure 18 shows the integration of embedded heat pipe in a satellite module and power unit. Two heat pipes are positioned in the middle of the module, underneath the printed circuit board (PCB), targeting the critical area where the majority of heat is expected to be generated [1]. The module is then replicated and assembled with all the electronic components (transformers, inductors, etc.) into a simplified version of a power unit that serves as part of the satellite's payload system. Finite-element analysis was conducted on the module, where the lattice was modeled as an equivalent homogeneous material with the properties derived from static tests, and the electronic components are considered as concentrated masses. A typical Power Spectral Density

Table 5 Lattice Dixon's method test results for the identification of fatigue limit

Stress level										
12 MPa					X					
10 MPa			O				X			O
8 MPa		O						O		

X = Failed samples; O = Run-out

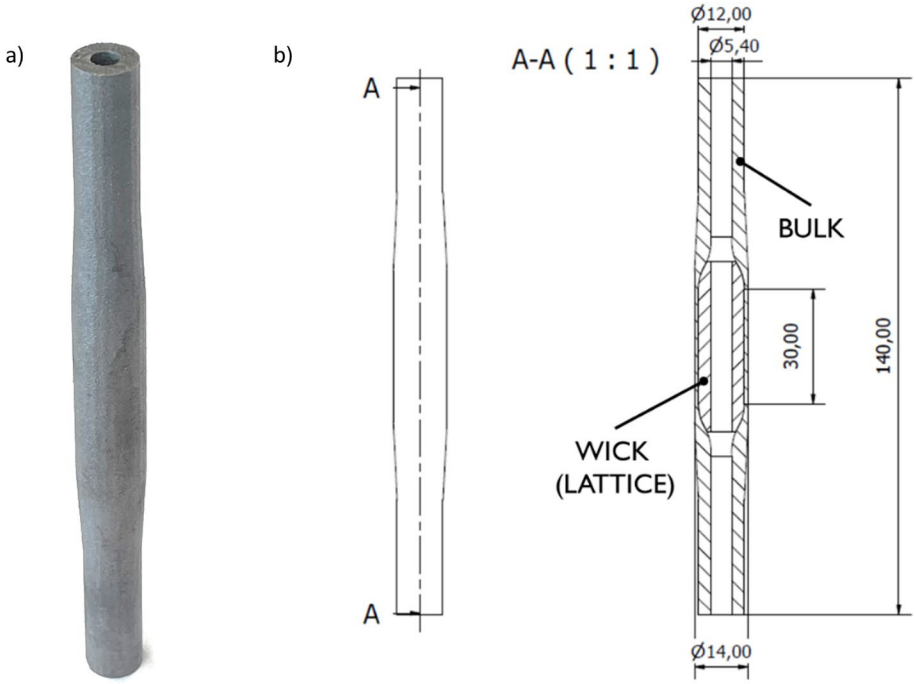

Fig. 16 Heat-pipe (component-like) specimen: **a** printed specimen and **b** technical drawings

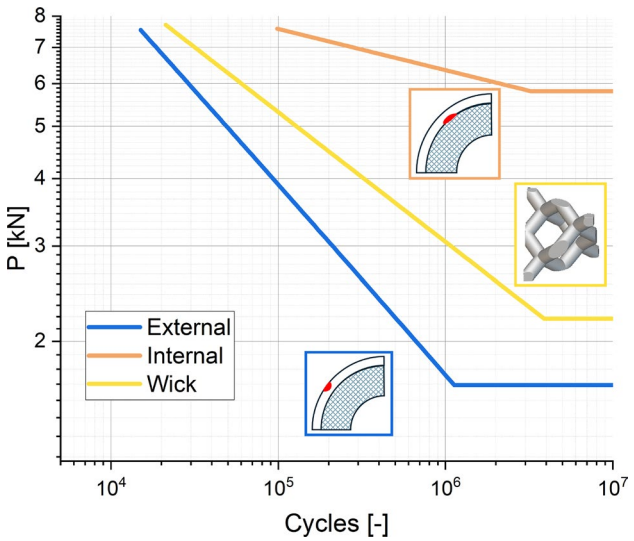

Fig. 17 Load-life prediction diagrams of the component based on the different failure location

(PSD) acceleration of space launch (Fig. 19a) was imposed to the system to obtain the stress state of the module. Linear tetrahedral elements (C3D4) are chosen to reduce the computational effort, while still assuring accuracy by means of mesh refinement in critical regions.

Following the same procedure used in [37], the PSD of the stress in the bulk material resulting from the analysis (Fig. 19b,c) was converted in the time domain using custom Matlab function imposing a total duration of 150 s (Fig. 19d). The resulted signal is characterized by a Root Mean Square (RMS) of 18 MPa in the bulk material, with a maximum stress of 90 MPa.

To investigate the damage induced by the random stress signal, the Miner's linear damage accumulation law was considered. The Miner's damage index was calculated starting from the stress signal decomposed in a series of cycles with a given amplitude ($\sigma_a^{[i]}$) with the use of a Rainflow's algorithm [38][39]. The damage index D is calculated with Eq. (8) [40], where $N^{[i]}$ is the number of

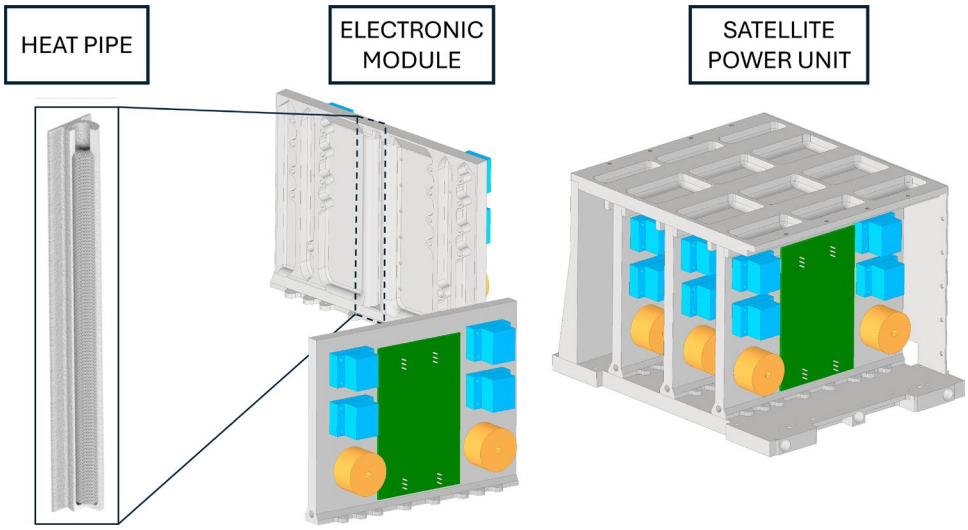

Fig. 18 Heat-pipe integration in an electronic module and in a satellite's power unit assembly. In gray components made in aluminum, in green the PCB, in orange the inductors, and in blue the transformers

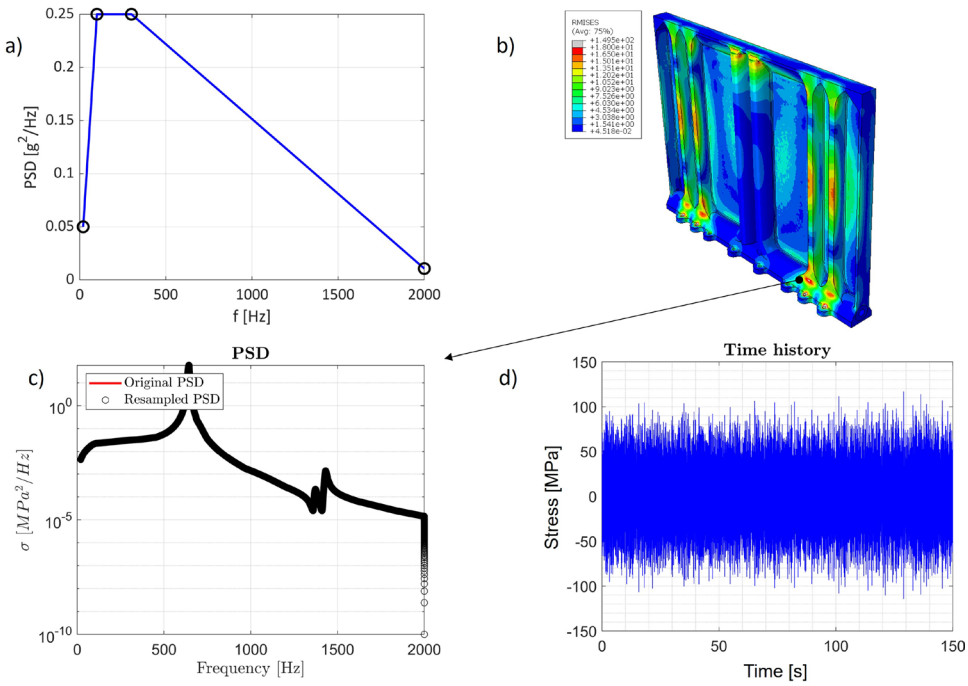

Fig. 19 **a** Typical PSD accelerations of a space launch, **b** results of the FE analysis simulating random vibration in terms of RMS of the Von-Mises stress, **c** PSD of the maximum stresses acting component, and **d** stress time history derived from PSD

cycles performed in the considered stress range and $N_f^{[i]}$ is the cycles at failure corresponding to the given stress amplitude of the ith cycle ($\sigma_a^{[i]}$), according to the SN diagram of the bulk material's external surface. For the case of stresses lower than the fatigue limit of the material, the Haibach assumption [41] was considered. A graphical representation of the damage index computation is presented in 20

$$D = \sum_i \frac{N^{[i]}}{N_f^{[i]}}. \tag{8}$$

The predicted accumulated damage for a single space launch is equal to 0.108, leading to a safety factor of 9, considering as failure an accumulated damage (D) equal to 1. Converting the applied stress history to the lattice using the load distribution, it is possible to compute the damage for the lattice structure for the same single space,

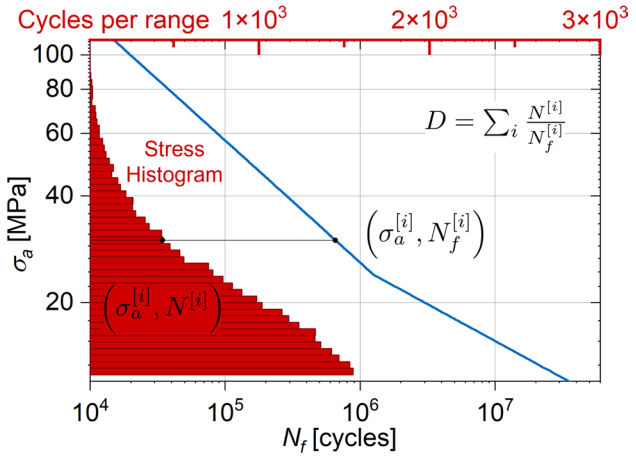

Fig. 20 Visual interpretation of Miner's damage calculation. In red the stress histogram corresponding to the stress history and in blue the SN diagram of the bulk material external surface

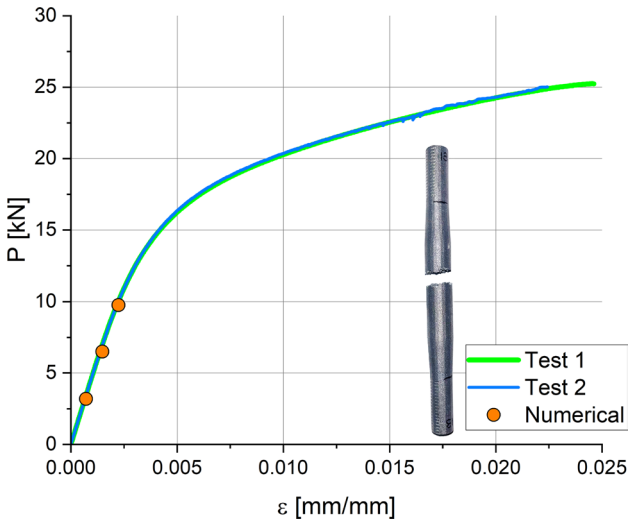

Fig. 21 Heat-pipe specimens' tensile tests alongside numerical points predicted by finite-element analysis and picture of a broken sample

using the SN diagram in Fig. 15. For a single launch, the accumulated damage is 0.0187.

4.4 Experimental validation on component-like specimens

Tensile test on component-like specimen were performed with the same modalities of the lattice tensile test on three specimen, although one was not considered valid, as it broke in the gripping region. The results are presented in Fig. 21 and Table 6. In Fig. 21, values of load strain predicted by the finite-element model are reported, to verify the goodness of considering the lattice as a homogeneous material with equivalent properties obtained from the tensile tests.

Table 6 Heat-pipe specimen's tensile tests results

	Test 1	Test 2	Mean
F_y (kN)	16.9	17	17
Load at rupture (kN)	25.2	24.9	25.1

Table 7 Identification of loads for fatigue testing of heat pipe specimen

	Load on specimen (kN)	Stress (MPa) on lattice	Stress on bulk (MPA)
Level 1	6.6	30	95.5
Level 2	4	18	57.8
Level 3	2.64	12	38.2

4.4.1 Constant amplitude fatigue

Fatigue tests were conducted using a servo-hydraulic MTS Landmark 25 kN machine until complete specimen failure. The data were post-processed to determine the number of cycles to failure, following the same procedures used for the lattice specimen. Similar to the previous study, three load levels were selected to determine the finite-life fatigue part of the curve, with three test repetitions at each level. The load levels were determined ensuring that the stress in the lattice of the heat pipe specimen corresponded to the stress levels tested in the fatigue analysis of the lattice specimen. The load levels used for the fatigue testing of the heat pipe specimen, along with the corresponding stresses on the bulk and lattice, are detailed in Table 7. Additionally, the fatigue strength of the component-like specimen was estimated using Dixon's method [36] (Table 8).

The obtained load-life diagram is compared with the predicted one in Fig. 22. The results show a good accordance between the predicted ones and the failure location which is confirmed to be the bulk material's external surface for all the tested specimens. To confirm the accuracy of the initial defect size estimation obtained from CT-scan analysis of a sample, the fracture surfaces of all tested specimens were examined under a Scanning Electron Microscope (SEM). An example of this is reported in Fig. 23. The depth of the *killer defect*, i.e., the defect originating fatigue failure, was measured and recorded for each specimen. The observed killer defects are lack of fusions originated from the contour scanning strategy, proven to worsen the material's fatigue properties [15]. Killer defects' depth values were fitted using a Largest Extreme Value Distribution (LEVD), as done in [42][28], to obtain a statistical distribution. The LEVD, depicted in Fig. 24, shows that the CT-scan predicted initial defect size of 0.35 mm corresponds to the 66th percentile of the killer defect distribution.

Table 8 Heat-pipe specimen Dixon method test results for the identification of fatigue load limit

Load level										
2.15 kN					X					
1.75 kN			O				X			O
1.35 kN		O							O	

X = Failed samples; O = Run-out

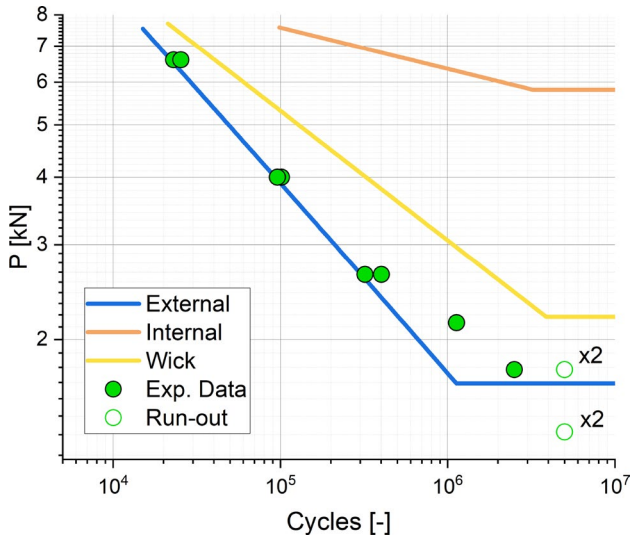

Fig. 22 Load-life curve at constant amplitude for the heat pipe specimen tested alongside the different prediction curves

4.4.2 Variable amplitude fatigue

Variable amplitude fatigue tests were conducted on the component-like specimen. The stress history considered in Fig. 19c was re-sampled at lower frequency for compatibility with the testing machine, and cycles with amplitudes below half the fatigue limit were removed to reduce experimental times, as done in [37]. The stress history was then converted to load and repeated n-times up to complete failure of the specimen. In addition, interrupted tests were performed to identify the presence of passing-through cracks before the complete failure of the specimens. A total of 6 tests were performed, and specifically, two tests were performed at complete failure (specimens #20 and #22 in Table 9), two test were interrupted at 9 repetitions (specimens #6 and #14), that is the safety factor predicted by the model, other tests were interrupted one at 7 (specimen #12) and one at 5 repetitions (specimen #11). Table 9 summarizes the performed tests at variable amplitude. The tests conducted at complete failure of the heat pipe showed that the heat pipe can sustain nine space launch repetitions. This is in line with the model's prevision, validating the accumulated damage at failure equal to one. Considering the interrupted tests, all specimens subjected to nine repetitions showed the presence of cracks with depth larger than the bulk thickness, thus indicating that the choice of an accumulated damage at failure equal to one is not valid to prevent fluid leakage. The test interrupted at seven repetitions revealed a crack with a depth of 0.75 mm, which is less than the bulk thickness (Fig. 25). This finding suggests that to prevent cracks exceeding the bulk thickness, an accumulated damage limit of 0.76 should be considered. Interestingly, the crack in the test interrupted at seven repetitions propagated beyond 0.5 mm, a depth at which the model predicted propagation would cease due to compressive residual stresses. This discrepancy challenges the assumptions made about the residual stress profile. Indeed, the presence of the defect—and the subsequent crack propagation—may alter the residual stress distribution at the crack tip, thus modifying the profile assumed in Fig. 11. Without sufficiently high compressive residual stresses, the crack is able to further propagate at its deepest point, eventually reaching the full thickness of the specimen.

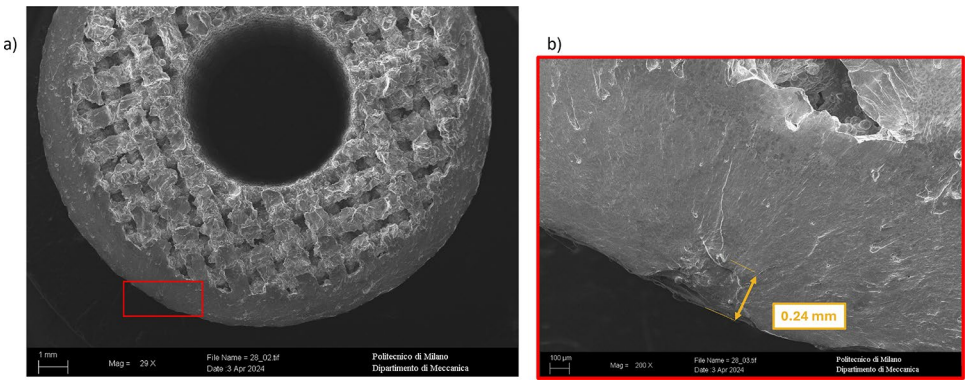

Fig. 23 **a** SEM image of the fracture surface of specimen tested at 2.64 kN; **b** zoom on the killer defect with the measure of the defect depth

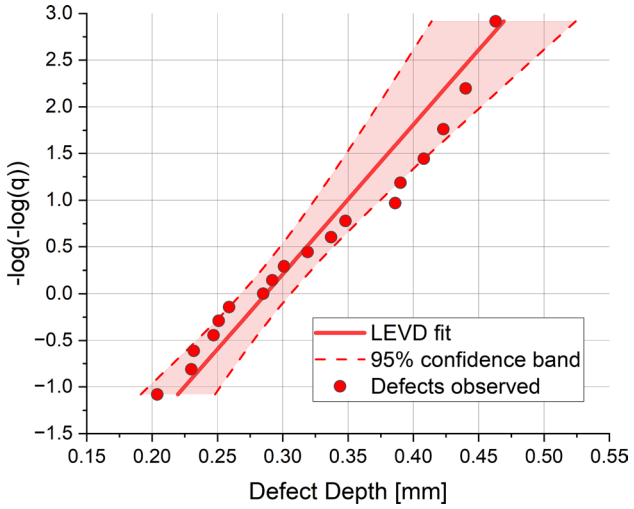

Fig. 24 LEVD fitting of the killer defects' depth

5 Conclusions

This paper presents the design and evaluation of an additively manufactured heat pipe with lattice structures as a wick. Different lattice structure were analyzed from a thermal point of view to identify the best-performing one in terms of heat dissipation and performance in against-gravity conditions. Given the industrial application in space satellites, the mechanical properties of the heat pipes were also assessed to ensure structural integrity under the load conditions induced by space launch vibrations.

The outcome of this applied research work is a heat pipe capable of dissipating 24 W at 0° inclination and maintains a correct functioning up to a 15° counter-gravity inclination with an input power of 18 W. The structural assessment of the heat pipe was done with a prediction model based on the properties of bulk AlSi10Mg, CT-scans, residual stress measurements, and experimental activity on the lattice structure, which was later compared with the results of an experimental campaign, performed on a component-like specimen. The predictive model successfully indicated the life of the component and its most critical region. Overall, the heat pipe showed the capability to sustain a load spectrum comparable with space launch vibrations with a safety factor of 9 with respect to the structural failure and a safety factor of 7 with respect to an operative failure condition. The validated predictive capability of the life prediction model lays the foundation for further enhancements and configurations of AM heat pipes with lattice structures, while also serving as a guideline for designing other space-related components. Future work will focus on integrating heat pipes into a fully operational satellite power unit module, aiming to validate the transferability of performance metrics assessed at the component level to a complete system assembly. Further research is needed to enhance the heat pipe's thermal and mechanical properties. This involves exploring alternative lattice topologies, sintered-style wicks, or hybrid designs for

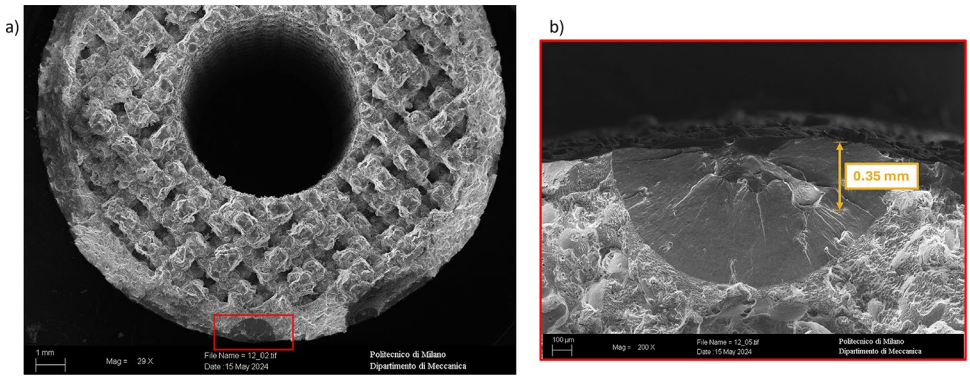

Fig. 25 **a** SEM image of the fracture surface of specimen 12 interrupted after 7 repetitions; **b** zoom on the largest non-passing-through cracks with highlighted the initial defect depth

Table 9 Variable amplitude fatigue tests on heat pipe specimen

Sample	RMS (MPa)	Repetitions	Damage at test termination	Through-the-thickness cracks
20	18	12.5	1.36	Yes (complete failure)
22	18	9	0.99	Yes (complete failure)
6	18	9	0.99	Yes
14	18	9	0.99	Yes
11	18	5	0.54	No
12	18	7	0.76	No

Specimens 20 and 22 up to complete failure

improved thermal performance. Simultaneously, to improve fatigue life, investigations should focus on optimizing printing parameters, scanning procedures, heat treatments, and surface treatments.

Acknowledgements Giovanni Brambati acknowledges funding from FSE REACT-EU, Programma Operativo Nazionale Ricerca e Innovazione 2014-2020 (CCI2014IT16M2OP005), Azione IV.5 "Dottorati su tematiche Green" (DOT1316301-12). The authors would like to express all their gratitude to the late Professor Alfonso Niro, for his contributions, dedication and insights that will continue to be an inspiration.

Author contributions G.B.: Methodology, Investigation, Data-curation, Visualisation, Writing—original draft. L.V.: Conceptualization, Investigation, Data-curation, Visualisation, Writing—review and editing. M. G.: Conceptualization, Methodology, Supervision, Writing—review and editing. E.C.: Supervision, Project administration, Funding. A.N.: Supervision, Resources, Project administration, Funding acquisition, Writing—review and editing. S.F.: Methodology, Supervision, Resources, Project administration, Funding acquisition, Writing—review and editing.

Funding Open access funding provided by Politecnico di Milano within the CRUI-CARE Agreement.

Data availability Data is provided within the manuscript.

Declarations

Conflict of interest The authors have declared that there is no conflict of interest.

Open Access This article is licensed under a Creative Commons Attribution 4.0 International License, which permits use, sharing, adaptation, distribution and reproduction in any medium or format, as long as you give appropriate credit to the original author(s) and the source, provide a link to the Creative Commons licence, and indicate if changes were made. The images or other third party material in this article are included in the article's Creative Commons licence, unless indicated otherwise in a credit line to the material. If material is not included in the article's Creative Commons licence and your intended use is not permitted by statutory regulation or exceeds the permitted use, you will need to obtain permission directly from the copyright holder. To view a copy of this licence, visit http://creativecommons.org/licenses/by/4.0/.

References

1. Moore AL, Shi L (2014) Emerging challenges and materials for thermal management of electronics. Elsevier. https://doi.org/10.1016/j.mattod.2014.04.003
2. Shukla K et al (2015) Heat pipe for aerospace applications-an overview. J Electron Cool Therm Control 5(01):1
3. Ghidini T, Grasso M, Gumpinger J, Makaya A, Colosimo BM (2023) Additive manufacturing in the new space economy: current achievements and future perspectives. Progress Aerosp Sci. https://doi.org/10.1016/j.paerosci.2023.100959
4. Elnaggar M, Edwan E (2016) Heat pipes for computer cooling applications. Electron Cool 51
5. Caruana R, Gallazzi L, Iazurlo R, Marcovati M, Guilizzoni M (2022) A multi-node lumped parameter model including gravity and real gas effects for steady and transient analysis of heat pipes. Fluids. https://doi.org/10.3390/fluids7030109
6. Tang H, Xie Y, Xia L, Tang Y, Sun Y (2023) Review on the fabrication of surface functional structures for enhancing heat transfer of heat pipes. Elsevier. https://doi.org/10.1016/j.applthermaleng.2023.120337
7. Jafari D, Wits WW (2018) The utilization of selective laser melting technology on heat transfer devices for thermal energy conversion applications: a review. Elsevier. https://doi.org/10.1016/j.rser.2018.03.109
8. Jafari D, Wits WW, Geurts BJ (2018) Metal 3D-printed wick structures for heat pipe application: capillary performance analysis. Appl Therm Eng 143:403–414. https://doi.org/10.1016/j.applthermaleng.2018.07.111
9. Jafari D, Wits WW, Vaneker THJ, Demir AG, Previtali B, Geurts BJ, Gibson I (2020) Pulsed mode selective laser melting of porous structures: structural and thermophysical characterization. Addit Manuf 35:25. https://doi.org/10.1016/j.addma.2020.101263
10. Robinson AJ, Colenbrander J, Deaville T, Durfee J, Kempers R (2021) A wicked heat pipe fabricated using metal additive manufacturing. Int J Thermofluids 12:25. https://doi.org/10.1016/j.ijft.2021.100117
11. Ameli M, Agnew B, Leung PS, Ng B, Sutcliffe CJ, Singh J, McGlen R (2013) A novel method for manufacturing sintered aluminium heat pipes (SAHP). Appl Therm Eng 52:498–504. https://doi.org/10.1016/j.applthermaleng.2012.12.011
12. Masoud Ameli S (2012) Additive layer manufactured sinter-style aluminium/ammonia heat pipes. Ph.D. thesis, Northumbria University. https://nrl.northumbria.ac.uk/id/eprint/16880
13. McGlen RJ (2021) An introduction to additive manufactured heat pipe technology and advanced thermal management products. Therm Sci Eng Progress. https://doi.org/10.1016/j.tsep.2021.100941
14. Sanaei N, Fatemi A (2021) Defects in additive manufactured metals and their effect on fatigue performance: a state-of-the-art review. Progress Mater Sci. https://doi.org/10.1016/j.pmatsci.2020.100724
15. Beevers E, Brandão AD, Gumpinger J, Gschweitl M, Seyfert C, Hofbauer P, Rohr T, Ghidini T (2018) Fatigue properties and material characteristics of additively manufactured AlSi10mg—effect of the contour parameter on the microstructure, density, residual stress, roughness and mechanical properties. Int J Fatigue 117:148–162. https://doi.org/10.1016/j.ijfatigue.2018.08.023
16. Edwards P, O'Conner A, Ramulu M (2013) Electron beam additive manufacturing of titanium components: properties and performance. J Manuf Sci Eng 135:25. https://doi.org/10.1115/1.4025773
17. Leuders S, Meiners S, Wu L, Taube A, Tröster T, Niendorf T (2017) Structural components manufactured by selective laser melting and investment casting-impact of the process route on the damage mechanism under cyclic loading. J Mater Process Technol 248:130–142. https://doi.org/10.1016/j.jmatprotec.2017.04.026
18. Beretta S, Patriarca L, Gargourimotlagh M, Hardaker A, Brackett D, Salimian M, Gumpinger J, Ghidini T (2022) A benchmark activity on the fatigue life assessment of AlSi10mg components manufactured by L-PBF. Mater Des 218:25. https://doi.org/10.1016/j.matdes.2022.110713
19. Gavazzoni M, Beretta S, Boniotti L, Carmine ED, Gallazzi L, Iazurlo R, Foletti S (2023) Structural assessment of a multi-functional additively manufactured space component with bulk-lattice hybrid architecture. Thin-Walled Struct 192:25. https://doi.org/10.1016/j.tws.2023.111158
20. ECSS-E-ST-32-01C—Space engineering: fracture control. European Cooperation for Space Standardization (2021)

21. Cutolo A, Beevers E, Van Hooreweder B (2023) A design strategy to enhance the mechanical response of diamond-based lattice structures produced by laser powder bed fusion. Mater Sci Eng A 876:145120. https://doi.org/10.1016/j.msea.2023.145120
22. Vitali L, Brambati G, Caruana R, Foletti S, Guilizzoni M, Niro A (2024) Permeability measurement of a 3D-printed alsi10mg porous medium: comparisons between first results with different experimental and numerical techniques. J Phys Conf Ser 2685(1):012052. https://doi.org/10.1088/1742-6596/2685/1/012052
23. Vitali L, Menini S, Guilizzoni M, Niro A (2024) Thermal performance against gravity of an AlSi10 am heat pipe with a diamond lattice structure. J Phys Conf Ser. https://doi.org/10.1088/1742-6596/2766/1/012020
24. Newman JC (1984) A crack opening stress equation for fatigue crack growth. Int J Fract 244(4):1573–2673. https://doi.org/10.1007/BF00020751
25. El Haddad MH, Topper TH, Smith KN (1979) Prediction of non propagating cracks. Eng Fract Mech 11(3):573–584. https://doi.org/10.1016/0013-7944(79)90081-X
26. NASGRO Reference Manual Version 8.1. South West Research Institute (2016)
27. Barricelli L, Patriarca L, du Plessis A, Beretta S (2023) Orientation-dependent fatigue assessment of Ti6Al4v manufactured by L-PBF: size of surface features and shielding effect. Int J Fatigue 168:107401. https://doi.org/10.1016/j.ijfatigue.2022.107401
28. Sausto F, Tezzele C, Beretta S (2022) Analysis of fatigue strength of L-PBF AlSi10mg with different surface post-processes: effect of residual stresses. Metals 12(6):25. https://doi.org/10.3390/met12060898
29. Smith DJ, Farrahi GH, Zhu WX, McMahon CA (2001) Experimental measurement and finite element simulation of the interaction between residual stresses and mechanical loading. Int J Fatigue 23(4):293–302. https://doi.org/10.1016/S0142-1123(00)00104-3
30. Beghini M, Bertini L (1990) Fatigue crack propagation through residual stress fields with closure phenomena. Eng Fract Mech 36(3):379–387. https://doi.org/10.1016/0013-7944(90)90285-O
31. Inc.: nTop. https://ntop.com. Release 4.1
32. Gavazzoni M, Boniotti L, Foletti S (2021) Influence of specimen size on the mechanical properties of microlattices obtained by selective laser melting. Proc Inst Mech Eng C J Mech Eng Sci 235(10):1774–1787. https://doi.org/10.1177/0954406219869741
33. ISO 13314—Mechanical testing of metals—Ductility testing—Compression test for porous and cellular metals. ISO (2011)
34. E8/E8M: standard test methods for tension testing of metallic materials. ASTM International (2022)
35. E739-10: standard practice for statistical analysis of linear or linearized stress-life (SN) and strain-life (eN) fatigue data. ASTM International (2015)
36. Dixon WJ, Massey FJ (1969) Introduction to statistical analysis. McGraw-Hill
37. Gavazzoni M, Beretta S, Foletti S (2022) Response of an aluminium Schwarz triply periodic minimal surface lattice structure under constant amplitude and random fatigue. Int J Fatigue. https://doi.org/10.1016/j.ijfatigue.2022.107020
38. Standard practices for cycle counting in fatigue analysis. ASTM (2011)
39. Pisati M, Corneo MG, Beretta S, Riva E, Braghin F, Foletti S (2021) Numerical and experimental investigation of cumulative fatigue damage under random dynamic cyclic loads of lattice structures manufactured by laser powder bed fusion. Metals 11(9):25. https://doi.org/10.3390/met11091395
40. Eurocode 9: design of aluminium structures—Part 1-3: structures susceptible to fatigue. European Commitee for Standardization (2009)
41. Haibach E (2006) Betriebsfestigkeit. Springer
42. Beretta S (2021) More than 25 years of extreme value statistics for defects: fundamentals, historical developments, recent applications. Int J Fatigue 151:106407. https://doi.org/10.1016/j.ijfatigue.2021.106407

Publisher's Note Springer Nature remains neutral with regard to jurisdictional claims in published maps and institutional affiliations.

Authors and Affiliations

Giovanni Brambati[1] · Luigi Vitali[2] · Manfredo Guilizzoni[2] · Emmanuel Caplanne[3] · Alfonso Niro[2] · Stefano Foletti[1]

✉ Giovanni Brambati
giovanni.brambati@polimi.it

Luigi Vitali
luigi.vitali@polimi.it

Manfredo Guilizzoni
manfredo.guilizzoni@polimi.it

Emmanuel Caplanne
emmanuel.caplanne@esa.int

Alfonso Niro
alfonso.niro@polimi.it

Stefano Foletti
stefano.foletti@polimi.it

[1] Department of Mechanical Engineering, Politecnico di Milano, Milan, Italy

[2] Department of Energy, Politecnico di Milano, Milan, Italy

[3] European Space Research and Technology Centre, Noordwijk-Binnen, The Netherlands